

Disulfide-constrained Fabs overcome target size limitation for high-resolution single particle cryoEM

Received: 5 April 2024

Accepted: 28 August 2025

Published online: 30 September 2025



Jennifer E. Kung^{1,3}, Matthew C. Johnson¹, Dmitry Tegunov¹, Christine C. Jao¹, Ping Wu¹, Angela Oh¹, May Lin², Jose M. Daria², Christopher M. Koth^{1,3}, Christopher P. Arthur^{1,4}, Alexis Rohou¹ & Jawahar Sudhamsu¹✉

High-resolution protein structures are essential for understanding biological mechanisms and drug discovery. While cryoEM has revolutionized structure determination of large protein complexes, most disease-related proteins are small (<50 kDa) and challenging to resolve due to low signal-to-noise ratios and alignment difficulties. Current scaffold protein strategies increase target size but suffer from inherent flexibility, resulting in poorly resolved targets compared to scaffolds. We present an iteratively engineered molecular design transforming antibody fragments (Fabs) into conformationally Rigid Fabs that enable high-resolution structure determination of small proteins (~20 kDa). This design introduces strategic disulfide bonds, creating well-folded, rigidly constrained Fabs applicable across various species, frameworks, and chimeric constructs. Rigid Fabs enabled high-resolution cryoEM structures (2.3–2.5 Å) of two small proteins: Ang2 (26 kDa) and KRAS (21 kDa). Our disulfide-constrained Rigid Fab strategy provides a general approach for overcoming target size limitation of single-particle cryoEM.

Technological advances in cryogenic electron microscopy (cryoEM) have enabled the determination of high-resolution structures of large proteins and protein complexes¹. Solving the structures of small proteins (<50 kDa), however, remains a major challenge, as their lack of distinctive low-frequency structural features and the low signal-to-noise ratio in cryoEM images preclude accurate single-particle image alignment². Yet, most proteins in both prokaryotic and eukaryotic cells, including many drug targets, are smaller than 50 kDa³. Consequently, this powerful technique remains largely inaccessible for a vast proportion of the proteome.

Several approaches have been proposed to address this problem^{4–12}. Most of these seek to increase the apparent size of the small protein by designing another protein, a “structure chaperone”, that binds with high affinity to the small protein. Structure chaperones, such as designed ankyrin repeat proteins (DARPs), nanobodies, or

Fabs, can be evolved using in vivo and in vitro methods to bind to specific targets. The small size (~15 kDa) of DARPs and nanobodies, however, limits their use as structure chaperones for cryoEM of small targets. To overcome this limitation, both nanobodies and DARPs have been fused or bound to other proteins to produce elaborate scaffolds, such as “legobodies”¹³, “pro-macrobodies”⁹, “megabodies”¹⁴, and self-assembling protein cages^{5,7}, of sufficient size to visualize a small protein of interest. However, inherent flexibility of the resulting fusion proteins and assemblies^{4,5,15} limits the overall resolution of the small target protein, which is often poorly resolved relative to the structure chaperone (Supplementary Fig. 1).

Fabs, on the other hand, possess several favorable properties that make them an attractive option as structure chaperones: (1) Fabs can be discovered using well-established methods to bind almost any target with high affinity; (2) at ~50 kDa, Fabs by themselves are

¹Department of Structural Biology, Genentech Inc., South San Francisco, CA, USA. ²Department of Protein Chemistry, Genentech Inc., South San Francisco, CA, USA. ³Present address: Denali Therapeutics Inc., South San Francisco, CA, USA. ⁴Present address: FairJourney Biologics, San Diego, CA, USA.

✉ e-mail: sudhamsu.jawahar@gene.com

theoretically large enough to be resolved to high resolution via cryoEM¹⁶; (3) their distinctive shape provides a recognizable feature that facilitates accurate image alignment¹⁷. The primary limitation of Fabs as structure chaperones for cryoEM has been their inherent conformational flexibility¹⁸.

In this work, we apply iterative structure-guided protein engineering to design Fabs with reduced flexibility by introducing new disulfide bonds at strategic locations. We first assess the flexibility of various designs by solving cryoEM structures of relatively large antigen-Fab complexes and arrive at Fab designs that are conformationally rigid. We then translate these designs to Fabs against two small targets, Ang2 (26 kDa) and KRAS (21 kDa), and demonstrate that Rigid Fabs can enable high-resolution (~2.3–2.5 Å) structure determination of both of these small proteins using cryoEM. Our designs are transferable to practically any Fab against any target and should facilitate high resolution structure determination of many small proteins.

Results

Design, iteration and characterization of Rigid Fabs

Crystal structures of Fabs have revealed that there is a high degree of variability in the elbow angle between the variable and constant domains (115–225°) (Supplementary Fig. 2A)¹⁸. This flexibility frequently causes the constant domain of the Fab to be poorly resolved in cryoEM maps, and masks are often applied during refinement to exclude the Fab constant domain in order to achieve higher resolution at the Fab-antigen interface for large antigen-Fab complexes. Thus, only the ~25 kDa variable domain of the Fab is fully utilized in these cases to aid in image alignment. If the Fab were conformationally rigid with a distinctive shape, however, including the constant domain would (1) increase the overall ordered size of the particle by ~50 kDa, (2) alleviate the need for a mask to discount the constant domain, and (3) improve image alignment, leading to improved resolution of the constant domain and of the antigen-Fab complex overall. For a truly conformationally rigid Fab, the local resolution throughout the Fab would be expected to be relatively uniform.

Previous attempts to generate conformationally rigid Fabs utilized phage display to shorten and mutate the heavy chain (HC) elbow of the Herceptin Fab framework, and clones were selected based on their thermal stability¹¹. However, use of Fabs with these modifications in cryoEM studies revealed that they are still quite flexible^{12,19–22} (Supplementary Fig. 1F). To generate truly conformationally rigid Fabs, we sought protein engineering solutions to restrict the flexibility between the variable and constant domains that could be easily transferred between Fabs from different species, frameworks, as well as chimeric Fabs with variable and constant domains from different species.

Our analysis of structural alignments of existing crystal structures of Fabs from various species and frameworks revealed that rabbit Fabs are naturally less flexible than human or murine Fabs (Supplementary Fig. 2A and Supplementary Table 1). This reduced flexibility is likely due to an interdomain disulfide between residues C80 and C171 (Kabat numbering) in the light chain (LC) elbow²³. Structural analysis indicated that mutation of the corresponding residues in human Fabs, P80 and S171, to cysteine could allow for disulfide bond formation. We hypothesized that stabilizing a conformation observed fairly often in crystal structures of Fabs by introducing additional disulfide bonds in the elbow region could result in Fabs that are conformationally even more rigid (Fig. 1A). We analyzed structures of Fabs in the Protein Data Bank (PDB) and identified additional pairs of conserved residues (E81:S168, F83:Q166, I106:S171 in the LC and L11:P151, T110:P151 in the HC, anti-Tryptase Fab in 6VVU as reference) that were in close proximity with C β -C β distance ≤ 5.5 Å and oriented such that cysteine mutations may allow formation of disulfide bonds connecting the variable and constant domains (Supplementary Fig. 2B).

To assess the rigidity of the Fab designs, we chose human β -tryptase (120 kDa) and E104.v1, an anti-tryptase Fab that forms a 4:4, ~320 kDa complex with tryptase for which a 3.0 Å crystal structure is available²⁴. Tryptase as a model system offers two advantages: (1) It forms a symmetric tetramer, which makes for easier data processing and (2) at ~120 kDa, its structure can be solved at high resolution using cryoEM. We hoped this would then allow us to directly assess the rigidity of wild type or rigid Fab variants when bound to tryptase. Using this large, symmetric complex, we sought to identify the best design for a rigid Fab, with a view to later applying the design to Fabs targeting smaller antigens. We mutated the residue pairs mentioned earlier to cysteines in E104.v1 to generate Fabs that contained an elbow disulfide in their LC, HC, or both. Expression levels of the Fab variants were comparable to wild type (WT), and intact protein LC-MS indicated that each Fab had the expected additional number of disulfide bonds. Biolayer interferometry (BLI) showed that all Fab variants exhibited identical binding affinity and kinetics as E104.v1.WT and formed a 4:4 complex with tryptase (Supplementary Fig. 3).

We collected cryoEM datasets for samples of the tryptase tetramer in complex with E104.v1.WT or with a construct containing two elbow disulfides (2DS) formed by variants L11C:P151C in the HC and P80C:S171C in the LC. For the WT dataset, we obtained a reconstruction with a resolution of 2.9 Å (Fig. 1C, Supplementary Fig. 4A–E and Supplementary Table 2). The tryptase tetramer was the best-resolved part of the structure, and the Fabs were relatively poorly resolved, especially their constant domains, consistent with the expected flexibility of WT Fab. From the 2DS dataset, we obtained a reconstruction with an improved resolution of 2.7 Å (Fig. 1D, Supplementary Fig. 4F–J and Supplementary Table 2) and higher local resolution in tryptase, as well as the Fab variable and constant domains, compared to the WT structure, indicating that the 2DS Fab was indeed less flexible than the WT Fab (Fig. 1C, D, G, H, K, L).

Though the 2DS Fab was more rigid than the WT Fab, the constant domains of the 2DS Fab were still less well resolved than the variable domains, indicating some flexibility remained in the 2DS Fab elbow. To generate Fabs that are more rigid, we identified additional sites in the Fab LC and HC elbows to introduce more disulfides to further constrain the conformation of the Fab (Fig. 1A and Supplementary Fig. 2C). The structure of the E104.v1.WT-tryptase complex (PDB code 6VVU) indicated that the mutations P40C:E165C in the LC could lead to disulfide formation. In the HC, L108 and P153 were too far apart (C β -C β distance = 6.3 Å) to allow for disulfide formation with L108C:P153C mutations. Since P153 is in a loop, we inserted a cysteine residue between E152 and P153 to lengthen the loop and position the new cysteine close enough to enable disulfide bond formation with L108C. This design, 4DS, contained a total of four intrachain disulfides in the elbow region, two in each chain (Fig. 1A). As with the 2DS Fabs, the various 4DS Fabs expressed at levels similar to E104.v1.WT, possessed all four engineered elbow disulfides as indicated by intact LC-MS analysis, and bound to tryptase with similar binding affinity and kinetics as E104.v1.WT (Supplementary Fig. 3). To further characterize these Fabs, we crystallized and solved structures of the 4DS Fab variants at a resolution of 2.0 Å (Supplementary Fig. 2E, F and Supplementary Table 3). The structures confirmed that all four elbow disulfides formed as designed. To determine whether the additional elbow disulfides in the 4DS Fab would further reduce flexibility, we collected a cryoEM dataset for the tryptase-4DS Fab complex and obtained a 3D reconstruction with a resolution of 2.5 Å (Fig. 1E, Supplementary Fig. 4K–O and Supplementary Table 2). Strikingly, in addition to the improved overall resolution, we observed notable improvements in local resolution throughout the structure including several well-resolved water molecules (Fig. 1E, I, M), and especially in the constant domains of the Fabs, demonstrating that the new disulfides in the 4DS Fab significantly increased the rigidity of the Fab.

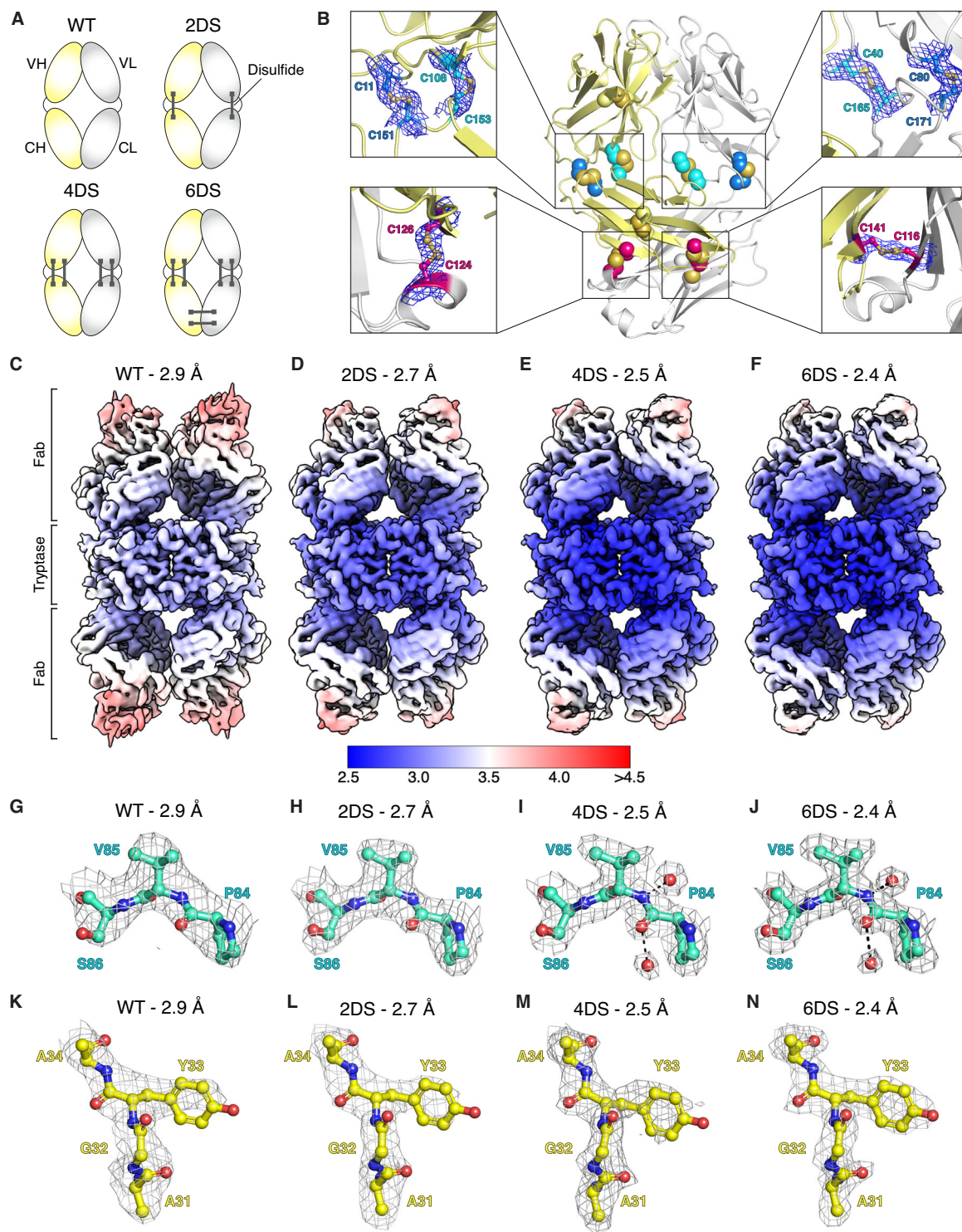


Fig. 1 | Design and characterization of Rigid Fabs. **A** Design of Rigid Fabs. To engineer Fabs that are conformationally rigid, two (2DS) or four (4DS) intrachain disulfides were introduced in the elbow region of both the light (gray) and heavy (yellow) chains to restrict the elbow angle between the variable and constant domains. Two additional interchain disulfides were introduced in the constant domain to further reduce the flexibility of this domain, leading to a Rigid Fab design containing six engineered disulfides (6DS). **B** Crystal structure of E104.v1.6DS Fab. Center, cartoon representation of E104.v1.6DS (HC, yellow; LC, gray) with disulfides

shown in spheres (2DS disulfides, cyan; 4DS disulfides, blue; 6DS disulfides, pink). Insets show electron density contoured at 1σ for each of the engineered disulfides. Maps of tryptase complexes with **C** WT, **D** 2DS, **E** 4DS, and **F** 6DS variants of the E104.v1 Fab colored by local resolution. EM density for selected map regions illustrating improvement in resolution with increasingly rigid constructs of E104.v1: **G–J** tryptase P84–S86 (green sticks) and **K–N** E104.v1 HC A31–A34 (yellow sticks) from the indicated tryptase–Fab structures.

We observed that the C-termini of the constant domains of the 4DS Fabs still retained some flexibility relative to the rest of the Fab (Fig. 1E) and sought to engineer this region of the Fab to further decrease flexibility. We examined our 4DS Fab crystal structures and identified additional sites in the constant domain where we could introduce interchain disulfides between the LC and HC (Supplementary Fig. 2D). We designed and expressed variants of E104.v1 that contained pairs of cysteine mutations at one or more of these sites in combination with the 4DS elbow mutations. All of the SDS/6DS Fabs bound to trypsin with similar binding affinity and kinetics as E104.v1.WT (Supplementary Fig. 3), demonstrating that the constant domain mutations also do not negatively affect the ability of the Fab to bind antigen. Furthermore, crystal structures of a 5DS (F116C^{LC}:A141C^{HC}) and a 6DS (F116C^{LC}:A141C^{HC} and Q124C^{LC}:F126C^{HC}) Fab further confirmed proper formation of all engineered disulfides (Fig. 1B, Supplementary Fig. 2G and Supplementary Table 3). We collected a cryoEM dataset for the trypsin-6DS Fab complex and obtained a 3D reconstruction with an overall resolution of 2.4 Å (Fig. 1F, Supplementary Fig. 4P–T and Supplementary Table 2). Overall, the 6DS map was very similar to the 4DS map with some improvements in local resolution, especially at the C-termini of the constant domains, consistent with the interchain disulfides in the constant domain increasing the rigidity of that domain (Fig. 1F, J, N). Comparison of ResLog plots for each of the trypsin-Fab complexes further demonstrated that each additional pair of engineered disulfides in the Fab led to marked improvements in the quality of the data, while also reducing the number of particles required to achieve higher resolutions (Supplementary Fig. 4U)²⁵.

Rigid Fab designs increase rigidity of non-human and chimeric Fabs

In light of our success designing rigid versions of E104.v1, a fully humanized Fab, we speculated that the same designs could be applied to rigidify Fabs derived from other species or chimeric Fabs. We selected the murine Fab 7A9 and the human-mouse chimeric Fab fragment from Rituximab (RTX), which target the membrane proteins NavAb-Nav1.7 (chimeric) channel and CD20, respectively. Since previous high-resolution cryoEM structures of NavAb-Nav1.7 and CD20 bound to WT Fabs revealed inherent flexibility in both Fabs^{26,27}, these systems would allow for assessing rigidity of the Rigid Fab designs applied beyond human Fabs. We generated 4DS variants of both 7A9 and RTX Fabs, using cysteine mutations at the same exact positions (Kabat numbering) as those introduced in the E104.v1.4DS Fab. Intact LC/MS analysis indicated that all four elbow disulfides were formed in both 7A9.4DS and RTX.4DS Fabs. We then collected cryoEM datasets for each antigen bound to either the WT Fab or 4DS Fab (Fig. 2 and Supplementary Fig. 5). For NavAb-Nav1.7, which forms a 4:2 NavAb-Nav1.7-Fab complex, the overall resolution of the consensus 3D reconstructions for both the NavAb-Nav1.7-7A9.WT and NavAb-Nav1.7-7A9.4DS complexes was 2.6 Å (Fig. 2A, B, Supplementary Fig. 5, 6 and Supplementary Table 4). Local refinement with a mask around the Fabs in the 7A9.4DS complex led to greater improvements in local resolution compared to 7A9.WT, especially in the constant domain, consistent with 7A9.4DS having increased rigidity (Fig. 2A–F and Supplementary Fig. 5). Though the overall resolution of both structures was similar, these results indicate that the 4DS mutations identified in human Fabs can be directly applied to increase rigidity of murine Fabs.

For CD20, which forms a 2:2 CD20-RTX Fab complex, the overall resolution of the consensus 3D reconstructions for both the CD20-RTX.WT and CD20-RTX.4DS complexes was 2.6 Å (Fig. 2G, H, Supplementary Fig. 6 and Supplementary Table 4). The constant domains of the 4DS Fabs were resolved to a much higher resolution than the WT Fabs, confirming that the 4DS mutations did indeed render the Fab significantly more rigid than WT (Fig. 2G–L). This increased rigidity of

RTX.4DS appeared to lead to lower resolution of the portions of the CD20 transmembrane helices distal to the Fab binding site, compared to the map obtained for the RTX.WT complex (Supplementary Fig. 6). We suspect that this effect was in part due to the nature of the CD20-RTX complex, in which two Fabs bind to one side of the CD20 dimer and to each other. The rigidity and greater mass of the 4DS Fabs, combined with the relative intrinsic flexibility of CD20 and added alignment noise from the detergent micelle surrounding it, likely caused the Fabs to become very well aligned at the cost of alignment accuracy and resolution in the regions of CD20 distal from the Fabs during refinement. In the case of the WT complex, the flexibility of the Fabs caused the constant domains to have less weight in determining particle alignments, allowing for improved alignments for CD20 compared to the 4DS Fab complex. Iterative local refinements using masks to exclude the 4DS Fab constant domains, followed by exclusion of the entire Fab, led to significant improvements in the resolution of the intracellular side of the CD20 helices (Supplementary Fig. 6L). The consensus map and focused maps were combined to generate a composite map that had improved resolution at the Fab-CD20 interface, as well as throughout CD20. The same procedure was applied to the RTX.WT dataset, leading to a final composite map with similar overall resolution to the RTX.4DS composite map (Fig. 2G, H and Supplementary Fig. 6). Thus, even though the rigidity of the 4DS Fab initially led to lower resolution of the antigen, local refinements were able to ameliorate this effect. Our observation that the RTX.4DS Fab could so strongly drive particle alignments underscored the marked increase in rigidity of 4DS Fab variants relative to WT Fabs.

Overall, the increased rigidity observed for both the 4DS variants of the 7A9 and RTX Fabs demonstrated the modularity of the 4DS Rigid Fab design. The same set of mutations introduced in the humanized E104.v1.4DS Fab successfully resulted in conformationally rigid Fabs against other antigens, even for murine or chimeric Fabs like 7A9 and RTX, respectively.

Rigid Fabs enable high-resolution structures of small proteins

To date, there are only three cryoEM structures (9JQT, 9IHC, 9B2C) of Fabs in complex with monomeric antigens smaller than 30 kDa in the EMDB with resolutions of ≤ 3.0 Å or better and only nine unique monomeric antigen-Fab complexes (9JQT, 9E6K, 9IHC, 9B2C, 8BW0, 8XS3, 8WZE, 7F9W, 7URX) with resolutions better than ≤ 3.5 Å, underscoring the difficulty of using flexible WT Fabs to solve high-resolution structures of small antigens. We next sought to determine whether Rigid Fabs, given their moderate size, were sufficient to enable high resolution structures of even smaller antigens. To test this, we selected the cytokine Ang2 (26 kDa), an extracellular protein and the GTPase KRAS (21 kDa), an intracellular protein, both of which are monomeric, as targets and generated a 6DS variant of the anti-Ang2 Fab 5A12 and a 4DS variant of the anti-KRAS Fab 2H11 based on our designs for the 4DS and 6DS variants of the anti-trypsin Fab E104.v1^{28,29}.

High-resolution cryoEM structure of a 26 kDa cytokine

To evaluate if we could use Rigid Fabs to solve a high resolution cryoEM structure of Ang2, we first generated a 6DS variant of the 5A12 Fab by introducing cysteine mutations at the same positions as in the E104.v1.6DS Fab and assembled a 74 kDa Ang2-5A12.6DS Fab complex. To further increase the mass of the sample and improve our chances at obtaining a high-resolution structure, we also generated a fusion of the Protein A D domain to Protein G (ProA-ProG) and formed a ternary complex with 5A12.6DS bound to Ang2 (Supplementary Fig. 7A). We then collected a cryoEM dataset for this complex, but 2D class averages revealed that the vast majority of the particles contained only Ang2 and the 6DS Fab, suggesting that the affinity of ProA-ProG was not high enough to remain bound at the low sample concentrations used during grid freezing (Supplementary Fig. 7B). Despite the small size (74 kDa) of the Ang2-5A12.6DS complex, secondary structure in both

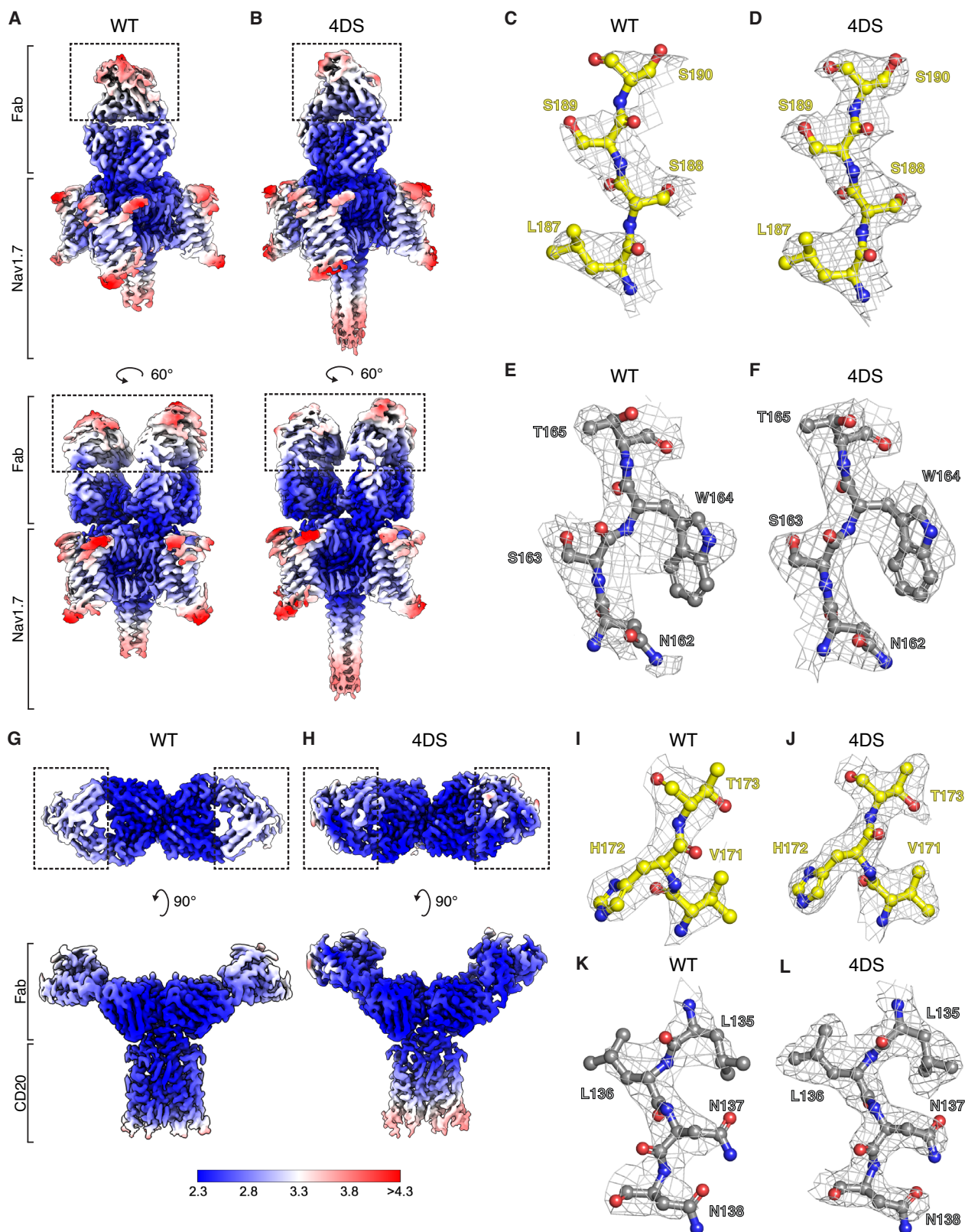


Fig. 2 | CryoEM structures of NavAb-Nav1.7-7A9 Fab and CD20-RTX Fab complexes. Composite cryoEM maps of NavAb-Nav1.7 complexes with **A** WT or **B** 4DS variants of the 7A9 Fab colored by local resolution. Dashed boxes indicate the constant domains of the Fabs. EM density for selected map regions illustrating improvements in resolution in the 7A9 HC (**C**, **D**) and LC (**E**, **F**) from the indicated

structures. Composite cryoEM maps of CD20 complexes with **G** WT or **H** 4DS variants of the rituximab (RTX) Fab colored by local resolution. Dashed boxes indicate the constant domains of the Fabs. EM density for selected map regions illustrating improvements in resolution in the RTX HC (**I**, **J**) or LC (**K**, **L**) from the indicated structures.

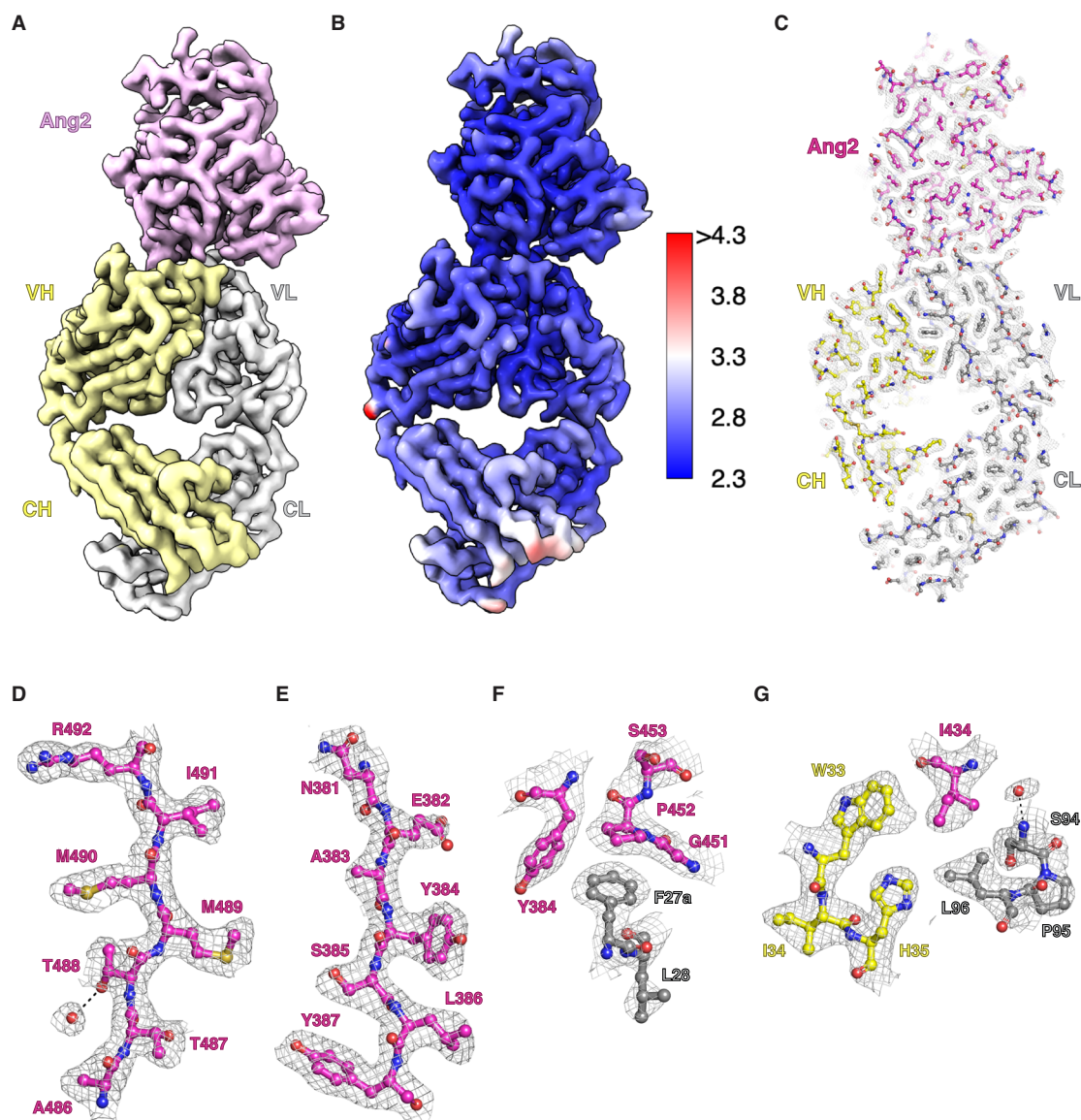


Fig. 3 | CryoEM structure of Ang2-5A12.6DS Fab complex. **A** CryoEM map of Ang2-5A12.6DS Fab complex at a resolution of 2.7 Å with Ang2 in pink, Fab HC in yellow, and LC in light gray. **B** CryoEM map of Ang2-5A12.6DS complex colored by

local resolution. EM density for the entire Ang2-5A12.6DS complex (**C**) and selected map regions (**D–G**) illustrating high resolution features, with Ang2 in magenta, RTX LC in gray, and HC in yellow.

Ang2 and the Fab were surprisingly clearly resolved in the 2D class averages. Through iterative rounds of heterogeneous refinement, particles containing ProA-ProG were removed, leaving a particle stack containing only the Ang2-5A12.6DS complex. These particles were then used to generate a 3D reconstruction with an overall resolution of 2.7 Å, with most regions of Ang2 reaching higher resolutions, up to 2.3 Å (Fig. 3B, Supplementary Fig. 7C–E and Supplementary Table 5). The local resolution is relatively uniform (~2.4–2.8 Å) throughout Ang2 and the Fab, consistent with 5A12.6DS being conformationally rigid (Fig. 3B). The overall structure of Ang2 is nearly identical to that observed in the 2.3 Å crystal structure of Ang2 and 5A12.WT (RMSD = 0.36 Å)²⁸. The resolution of the map enabled unambiguous placement of side chains in Ang2, the Fab, and the Ang2-Fab interface, and of several water molecules (Fig. 3C–G), highlighting that using a Rigid Fab design enabled high-resolution structure determination of the 26 kDa Ang2 by cryoEM.

To investigate the advantages conferred by the Rigid Fab compared to the WT Fab in obtaining a high resolution structure of a small protein like Ang2, we then conducted a head-to-head comparison by carefully preparing samples of Ang2 bound to either WT or 6DS Fab at

the same time using identical grid freezing conditions and collected datasets for grids of each sample with similar ice thickness and the same data collection parameters. Using the same image processing workflow and a similar number of particles (20,000), we obtained 3D reconstructions for both samples, with the 6DS sample achieving a higher overall resolution of 3.3 Å, while the WT sample reached an overall resolution of 3.7 Å. Focused refinement with a mask to exclude the Fab constant domain only led to minor improvements in both maps. ResLog analysis indicates that significantly fewer particles would be required for the 6DS sample compared to the WT sample to achieve similar resolution (Supplementary Fig. 8).

High-resolution cryoEM structure of a small molecule bound to 21 kDa KRAS

Next, we reasoned that Rigid Fabs could be used to accelerate structure-based drug design efforts by enabling high-resolution cryoEM structure determination of small molecule drug targets, many of which are <50 kDa and sometimes can be intractable for structure determination by crystallography or cryoEM. We chose the 21 kDa GTPase KRAS as a test case, since an anti-KRAS Fab has been

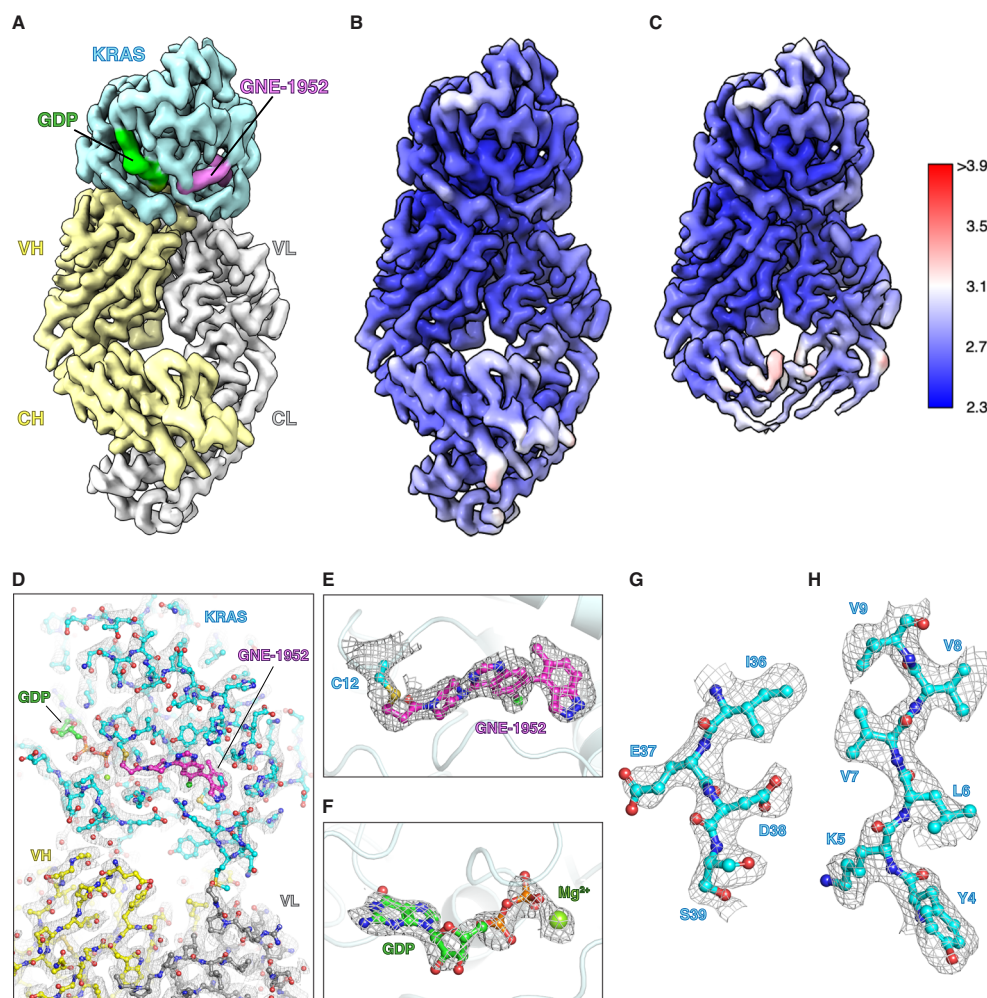


Fig. 4 | CryoEM structure of KRAS^{G12C}-GNE-1952-2H11.4DS Fab complex.

A CryoEM map of KRAS^{G12C}-GNE-1952-2H11.4DS Fab complex at a resolution of 2.8 Å with KRAS^{G12C} in cyan, GNE-1952 in pink, GDP in green, 2H11.6DS HC in yellow, and LC in light gray. **B** Map of KRAS^{G12C}-GNE-1952-2H11.4DS complex colored by local

resolution. **C** Locally refined cryoEM map of KRAS^{G12C}-GNE-1952-2H11.4DS complex colored by local resolution. EM density for the entire KRAS^{G12C}-GNE-1952-2H11.4DS complex (**D**), GNE-1952 covalently bound to C12 (**E**), GDP (**F**), and selected regions of KRAS^{G12C} (**G**, **H**) illustrating high resolution features.

reported²⁹. Unlike the Fabs described so far in the current work, the anti-KRAS Fab 2H11 contains a lambda LC rather than a kappa LC. Lambda LCs are slightly longer, which leads to a wider range of possible elbow angles¹⁸. Analysis of published crystal structures of 2H11 Fab-KRAS^{G12C} complexes indicated that this Fab is indeed highly flexible²⁹ and that the LC cysteine mutations used in our previous 2DS and 4DS designs would likely not be compatible with elbow disulfide formation in this Fab. To form the disulfide corresponding to the LC disulfide introduced in the 2DS design, we inserted a cysteine between N170 and N171 rather than a N171C mutation, as N171 was likely too far from S80 for disulfide formation (Supplementary Fig. 9A). For the second LC disulfide, we used the mutation K166C instead of Q167C since K166 was closer to P40 (Supplementary Fig. 9A). Using these mutations, we generated constructs for 4DS and 6DS variants of 2H11. While the 2H11.6DS Fab did not express, we were able to express and purify 2H11.4DS, and LC/MS indicated that all four elbow disulfides had formed. We proceeded to use 2H11.4DS to form a complex with KRAS^{G12C} conjugated to the covalent inhibitor GNE-1952 and collected a cryoEM dataset (Supplementary Fig. 9). This led to a 3D reconstruction with an overall resolution of 2.8 Å for the whole complex, with regions of KRAS and the Fab variable domain having local resolutions of ~2.5 Å (Fig. 4A–C, Supplementary Fig. 9C–H and Supplementary Table 5). The local resolution of the Fab constant domain was marginally lower than in the variable domain, unlike 5A12.6DS, consistent with 4DS Fabs

being slightly more flexible than 6DS Fabs. Local refinement with a mask to exclude the constant domain led to an overall resolution of 2.7 Å with improvements in local resolution in KRAS, the Fab variable domain, and the ligand-binding sites, with several regions reaching ~2.3 Å resolution (Fig. 4C). The overall structure of KRAS, GDP, and GNE-1952 in our work is nearly identical to the published crystal structure (RMSD = 0.67 Å)²⁹. Importantly, the high-resolution features at 2.3 Å in the ligand-binding sites for GDP and the inhibitor GNE-1952 enabled unambiguous placement of both ligands, as well as the covalent linkage between C12 and GNE-1952 (Fig. 4D–F). Sidechains throughout the KRAS^{G12C} portion of the structure were also very well-resolved (Fig. 4D, G, H).

Discussion

Computational methods for structure determination, such as AlphaFold^{30–32}, allow valuable modeling of the overall structures of proteins and their complexes. Such modeling is now routinely being used to generate useful hypotheses to advance our understanding of interactions of proteins with other molecules and to expedite structure determination by providing initial models as starting points for experimental maps from either crystallography or cryoEM. However, these models do not replace experimental structure determination³³. The need for accurate, experimental structure determination of proteins and protein complexes to high resolution continues to exist. Small proteins

(<50 kDa) encompass a vast majority of all known proteins, especially in the context of drug targets in humans and pathogens. While several of these proteins are amenable to high-resolution structure determination by x-ray crystallography, many others have had limited success due to low expression yields, low solubility, or lack of crystallizability. CryoEM circumvents these challenges, because it requires low protein amounts and concentrations, yet remains challenging when working with small proteins, which are plagued by low signal-to-noise ratio and lack distinctive features for particle alignment. While it is difficult to firmly compare merits of different chaperones described in literature, that are used in cryoEM, in this study, we demonstrate that Rigid Fabs increase the effective size of the target protein in a rigid manner and improve particle alignment and pose assignment. This results in high-resolution structure determination of proteins as small as ~21 kDa, revealing features, such as water molecules and unambiguous placement of specific conformations of protein side chains, atoms, and small ligands, like inhibitors and co-factors. The modularity of our Rigid Fab designs allows their straightforward application to nearly any existing Fab or newly discovered Fab independent of its source (species), framework or chimeric nature and against any target, making this powerful tool accessible to all researchers. This modularity would especially be impactful in pure research as well as drug discovery settings allowing: (1) structure determination of proteins which are intractable to existing methods due to various factors including size; (2) faster structure determination of antigen-Fab complex structures and epitope mapping for improved antibody discovery and optimization in early stages of immunization campaigns; (3) iterative structure-based drug design for small molecule drug targets that cannot be enabled using x-ray crystallography.

The modularity of the Rigid Fab designs is made possible by the highly conserved fold and architecture of Fabs across different species, such that one does not need a pre-existing structure of the Fab of interest in order to design a rigid version. Instead, sequence alignments with the Rigid Fabs presented in this study (Supplementary Fig. 10A, B) should be sufficient in most cases to identify sites to introduce the cysteine mutations needed to form disulfides to rigidify other Fabs. Furthermore, our Rigid Fab designs have resulted in Fabs that adopt a similar conformation (Supplementary Fig. 10C). A comparable conformation is observed fairly often in crystal structures of Fabs. Their inherent flexibility likely makes it possible for most Fabs to sample this conformation during expression and folding, enabling disulfide bond formation using the set of elbow and constant domain mutations from our designs. Our data suggests that the introduction of the described four disulfide bonds (4DS) in the Fab elbow region should suffice for high-resolution (~2.5 Å) structure determination of a small protein, but that introduction of six disulfide bonds (6DS) can further improve the resolution.

Rigid Fabs are likely to be most transformative in the study of small (<30 kDa) protein targets. For larger targets (e.g. ~130 kDa NavAb-Nav1.7 tetramer or ~45 kDa CD20 dimer), which likely feature more intrinsic flexibility than the Fab itself, we anticipate that Rigid Fab technology can also facilitate high-resolution structure determination at the Fab-antigen interface but may still need to be coupled with image processing strategies, such as focused refinements or flexibility analysis in order to achieve high resolutions throughout a large, flexible target. Alternatively, or as a complement to such an approach, one may deploy multiple Rigid Fabs against epitopes present on opposite “sides” of the target, in which case, the Fabs would aid not only in particle alignment, but also in 3D classification or flexibility analysis. None of these approaches should be needed, however, when the target proteins are suitably small and rigid. Rigid Fab technology expands the capability for structure determination of targets of sizes otherwise challenging by cryoEM. We anticipate that this will accelerate basic research into molecular mechanisms of action of proteins involved in pathways of interest, as well as speed up structure-guided drug discovery and optimization.

Methods

Recombinant protein expression and purification

Wild type and Rigid Fabs. C-terminally His6-tagged heavy chain and untagged light chain expression constructs (based on the pRK mammalian expression vector) were generated by gene synthesis and codon optimized for mammalian expression (Genscript). Fabs were expressed by transient transfection in CHO cells. Briefly, per 1 Liter of CHO cell culture at a density of 12 M cells/mL, the transfection mixture contained 3 mg DNA (1 mg coding DNA plasmid, 0.3 mg XBPIs DNA and 1.7 mg sheared herring sperm DNA) combined with 4.5 mL of PEI pro. Cells were cultured at 33 degrees C for 7 days in sortaREM medium with intermittent addition (100 mL/L of culture) of sortaRF 2.0 medium supplemented with 138 g/L Glucose. After harvest, the His-tagged Fabs were purified from the supernatant by nickel affinity chromatography (HisTrap Excel, Cytiva) in PBS equilibrated resin, followed by size exclusion chromatography (SEC) on a Superdex 200 column (Cytiva) equilibrated in 20 mM histidine acetate pH 5.5, 150 mM NaCl. The yields of various fab variants ranged from 1–10 mg per Liter of expression, with the 6DS fabs showing lower expression compared to other variants. The presence of the engineered disulfides in the Rigid Fab constructs was confirmed by intact protein LC/MS.

Trypsase. Constructs for human β -tryptase encoding residues I31-P275 with an N-terminal His tag followed by an enterokinase (EK) cleavage site were expressed and purified from *Trichoplusia ni* insect cells³⁴. Cultures were harvested 48 h post-infection. The supernatant media was filtered through a 0.22 μ m filter, and the His-tagged zymogen trypsin was purified by nickel affinity chromatography (Ni-NTA Superflow, Qiagen) followed by SEC on a Superdex 200 column (Cytiva) equilibrated in SEC buffer (10 mM MOPS pH 6.8, 2 M NaCl). Peak fractions were pooled and concentrated to 2 mg/mL prior to overnight cleavage with 0.1 mg/mL EK (New England Biolabs) at room temperature in 10 mM MOPS pH 6.8, 0.2 M NaCl, 0.5 mg/mL heparin (H3393, Sigma), which results in activation and tetramerization of trypsin. Tetrameric trypsin was purified on a Superdex 200 column equilibrated in SEC buffer.

Biotinylated trypsin was generated using a construct with a C-terminal Avi tag and coexpression with BirA to enable in vivo biotinylation. The biotinylated trypsin zymogen was purified via nickel affinity chromatography followed by SEC as described above. Addition of a single biotin was confirmed by intact protein LC/MS.

NavAb-Nav1.7 (chimeric) channel. Details of construct design for insect cell expression of Flag-tagged chimeric NavAb-Nav1.7³⁵ were repeated. Expression was performed in *T. ni* insect cells for 48 h. Two liters of insect cell paste were resuspended in 60 mL CytoBuster (#71009-4, EMD Millipore) supplemented with 1 μ g/mL benzonase and 1x protease inhibitor (Roche). The mixture was incubated at 22 °C for 5 min and transferred to 50 mL conical tubes. One % GDN (w/v) was added to solubilize samples. Samples were incubated with anti-Flag magnetic beads (Genscript, L00835) at 4 °C for 2 h with rotary mixing. To wash unbound proteins from the magnetic beads, a magnetic rack was used (L00723, Genscript). Beads were washed 4x with 10CV Wash Buffer containing 0.042% GDN. Proteins were eluted with an Elution Buffer containing 0.042% GDN and 150 μ g/mL Flag peptide. Fractions were pooled and separated on a Superose 6 10/300 column (Cytiva) equilibrated in Gel Filtration Buffer (10 mM Tris pH 8.0, 100 mM NaCl, 0.042% GDN).

CD20. Details of construct design for insect cell expression of His-tagged CD20²⁷ were followed. Expression was performed in *T. ni* insect cells for 48 h. Two liters of insect cell paste was resuspended in 60 mL cell resuspension buffer (25 mM Tris pH 7.5, 300 mM NaCl, 10% glycerol) supplemented with 1 μ g/mL benzonase and 1x protease inhibitor

(Roche). The mixture was incubated at 22 °C for 5 min and transferred to 50 mL conical tubes.

One % GDN/0.1% CHS (w/v) was added to solubilize samples, and as well as washed nickel magnetic beads. Samples were incubated with Ni-charged magnetic beads (L00295, Genscript) at 4 °C for 2 h with rotary mixing. To wash unbound proteins from the magnetic beads, a magnetic rack was used (L00723, Genscript). Beads were washed 4x with 10CV Wash Buffer containing 0.02% GDN/0.002% CHS. Proteins were eluted with an elution buffer containing 300 mM imidazole. Fractions were pooled and separated on a Superose 6 10/300 column (Cytiva) equilibrated in gel filtration buffer (25 mM Tris pH 7.5, 150 mM NaCl, 0.02% GDN/0.002% CHS).

Ang2. C-terminally His-tagged Ang2 (residues E277-F496) was expressed and purified from *T. ni* insect cells²⁸. Cultures were harvested 48 h post-infection. The supernatant media was filtered through a 0.22 µm filter, and the protein was purified by nickel affinity chromatography (HisTrap Excel, Cytiva) followed by SEC on a Superdex 200 column (Cytiva) equilibrated in 20 mM Tris pH 7.5, 150 mM NaCl.

ProA-ProG. To generate an N-terminally His-tagged construct for bacterial expression of a Protein A-Protein G (ProA-ProG) fusion protein, residues F100-K153 from Protein A and residues T368-G430 from Protein G were linked with a 3xGS linker. The ProA-ProG fusion protein was expressed in BL21(DE3) cells in TB autoinduction media for 48 h at 17 °C. Cell pellets were resuspended in lysis buffer (50 mM Tris pH 8.0, 500 mM NaCl, 10% glycerol) supplemented with 20 mM imidazole, 1 EDTA-free protease inhibitor tablet, 1 µg/mL benzonase, lysis detergents (0.3% Sb3-14 and 0.03% C7BzO), and 20 mg lysozyme. The solution was homogenized and incubated with 2 ml per 1 L pellet of Ni-charged MagBeads (L00295, Genscript) for 30 min at room temperature. To wash unbound proteins from the magnetic beads, a magnetic rack was used (L00723, Genscript). Beads were washed 4x with 10CV lysis buffer supplemented with 20 mM imidazole. The bound protein was eluted with a lysis buffer supplemented with 300 mM imidazole. The protein was then concentrated and purified via SEC on a Superdex 75 column (Cytiva) equilibrated in 20 mM Tris pH 7.5, 150 mM NaCl.

KRAS^{G12C}. A “Cys-light” construct of KRAS^{G12C} (residues M1-K169) was generated for *E. coli* expression by mutating all Cys residues except C12 to Ser. The protein was expressed in BL21(DE3) cells induced with 0.5 mM IPTG overnight at 16 °C. Cells were then harvested, resuspended in lysis buffer (50 mM HEPES pH 7.0, 300 mM NaCl, 5% glycerol, 5 mM MgCl₂, 10 µM GDP, 1 mM TCEP) supplemented with 1 mM PMSF, 1 µg/mL benzonase, and 1x protease inhibitor (Roche), and lysed using a microfluidizer. The clarified supernatant was passed over a NiNTA agarose column (Qiagen), and the protein was eluted with a lysis buffer supplemented with 300 mM imidazole. The eluted protein was dialyzed into dialysis buffer (50 mM HEPES pH 7.0, 300 mM NaCl, 5 mM MgCl₂, 10% glycerol, 1 mM TCEP, 10 µM GDP) and incubated overnight with TEV protease to cleave the His tag. The sample was passed again over a Ni-NTA column to remove uncleaved protein. The flowthrough was concentrated and purified via SEC on a Superdex 75 column (Cytiva) equilibrated in SEC buffer (50 mM HEPES pH 7.0, 100 mM NaCl, 1 mM MgCl₂, 1 mM TCEP, 10 µM GDP).

Biolayer interferometry

All binding assays were performed in 20 mM Tris pH 7.5, 150 mM NaCl, 0.1% BSA, 0.01% Tween20. Biotinylated tryptase was captured on streptavidin SA biosensors (Sartorius). Assays were performed in triplicate on an OctetRED384 (Fortebio, Octet Analysis studio Version 11.0+). Sensograms were normalized to a reference well containing only buffer. Equilibrium binding constants were determined by plotting the average response values versus Fab concentration and fitting

to a global one site-specific binding model in Prism (Graphpad) version 9.1.0.

Protein crystallization, data collection and processing

E104.v1.4DS S112F was crystallized at a concentration of 8 mg/mL via vapor diffusion in sitting well drops at 19 °C in 0.2 M Na citrate and 20% PEG 3350. Crystals were cryoprotected in mother liquor supplemented with 10% glycerol. Diffraction data were collected at the Advanced Light Source (ALS) beamline 5.0.2. Data were processed to a resolution of 2.0 Å in XDS, and phases were obtained through molecular replacement with Phaser, using E104v1.WT variable and constant domains from a crystal structure of the E104v1.WT-Tryptase complex (PDB: 6VVU, chains G and I) as search models.

E104.v1.4DS A114F was crystallized at a concentration of 10 mg/mL via vapor diffusion in sitting well drops at 19 °C in 0.1 M Na citrate pH 4.5 and 20% PEG 4000. Crystals were cryoprotected in mother liquor supplemented with 10% glycerol. Diffraction data were collected at the Advanced Light Source (ALS) beamline 5.0.2. Data were processed to a resolution of 2.01 Å in XDS³⁶, and phases were obtained through molecular replacement with Phaser, using the crystal structure of E104v1.4DS S112F as the search model.

E104.v1.5DS and E104v1.6DS were crystallized at concentrations of 10 mg/mL and 7 mg/mL, respectively via vapor diffusion in hanging well drops at 19 °C in 0.1 M Na Citrate pH 4.5 and 26% PEG 4000. Crystals were cryoprotected in mother liquor supplemented with 20% glycerol. Diffraction data were collected at Stanford Synchrotron Radiation Lightsource (SSRL) beamline 1.2.1. Data were processed to a resolution of 2.14 Å for E104.v1.5DS and 2.71 Å for E104.v1.6DS in XDS, and phases were obtained through molecular replacement with Phaser, using the crystal structure of E104v1.4DS A114F as the search model. Iterative rounds of model building and refinement were performed in COOT (0.9.6)³⁷ and Phenix (1.21rc1_5049)³⁸. Figures were generated using PyMOL (2.5.2).

CryoEM sample preparation, data acquisition, and data processing

Tryptase. Tryptase-Fab complexes were prepared by incubating tetrameric tryptase with a 2-fold molar excess of Fab on ice for 30 min. The tryptase-Fab complex was then separated via size exclusion chromatography on a Superdex 200 3.2/300 or Superose 6 3.2/300 column (Cytiva) equilibrated in 20 mM MOPS pH 5.5, 800 mM NaCl. The peak fraction was subjected to mild crosslinking with 2.5 mM BS3 (Thermo Fisher Scientific) at room temperature for 10 min. The crosslinking reaction was quenched by addition of 100 mM Tris pH 7.5. Four µL of this sample were then applied to a grid, blotted in a VitroBot MarkIV (ThermoFisher Scientific) at 4 °C and 100% humidity, using a blotting time of 3 s and a blot force of 7, and plunge-frozen in liquid ethane cooled by liquid nitrogen. The tryptase-E104.v1.WT Fab complex was applied to a glow-discharged Quantifoil R0.6/1 Cu400 holey carbon grid (Electron Microscopy Sciences). The tryptase-E104.v1.2DS complex was applied to a glow-discharged Quantifoil R0.6/1 Au300 holey carbon grid (Electron Microscopy Sciences). The tryptase-E104.v1.4DS and tryptase-E104.v1.6DS complexes were applied to Quantifoil R0.6/1 Au300 holey carbon grids treated overnight with a thiol-reactive, self-assembling reaction mixture of 4 mM mono-thiolalkane(C11)PEG6-OH (11-mercaptopoundecyl) hexaethyleneglycol (SPT-0011P6, SensoPath Technologies Inc., Bozeman, MT)³⁹. Before application of the protein, the grids were removed from the SAM solution and rinsed with ethanol.

Movie stacks for tryptase-E104.v1.WT Fab were collected using SerialEM (v4.1.0)⁴⁰ on a Titan Krios (Thermo Fisher Scientific) operated at 300 kV and equipped with a BioQuantum energy filter operated with a 20 eV energy slit with a K2 Summit direct electron detector camera (Gatan). Images were recorded at a nominal magnification of ×165,000, corresponding to 0.824 Å per pixel. Each image stack

contains 50 frames recorded every 0.2 s giving an accumulated dose of 54 e/Å² and a total exposure time of 10 s. Images were recorded with a set defocus range of 0.5 to 1.5 μm.

Movie stacks for tryptase-E104.v1.2DS, tryptase-E104.v1.4DS, and tryptase-E104.v1.6DS were collected using SerialEM (v4 1.0)⁴⁰ on a Titan Krios (Thermo Fisher Scientific) operated at 300 kV and equipped with a BioQuantum energy filter operated with a 20 eV energy slit with a K3 Summit direct electron detector camera (Gatan). Images were recorded in EFTEM mode at a magnification of 105,000x corresponding to 0.838 Å per pixel, using a 20 eV energy slit. Each image stack contains 60 frames recorded every 0.05 s for an accumulated dose of ~65 e/Å² and a total exposure time of 3 s. Images were recorded with a set defocus range of 0.5 to 1.5 μm.

For all four tryptase-Fab complexes, image processing was performed as described in Supplementary Fig. 4. Motion correction, CTF estimation, and particle picking were performed in cisTEM⁴¹. Particles were extracted from micrographs with CTF fit resolution less than 6 Å with a box size of 400 px and imported into cryoSPARC (v3.2.2)⁴². The particles were binned to a box size of 128 px and subjected to 2D classification to remove junk particles. The remaining particles were subjected to iterative rounds of multi-class ab initio reconstruction and heterogeneous refinement. The quality of the particles in the best classes was evaluated by running non-uniform refinement. The unbinned particles in the best class were then exported back into cisTEM. Prior to export, the Particle Sets tool in cryoSPARC (v3.2.2) was used to randomly select a subset of the best particles from the 2DS, 4DS, and 6DS datasets in order to match the final number of particles in the WT dataset. In cisTEM, 3D refinement was performed using Auto-refine, using a low-pass filtered map from non-uniform refinement in cryoSPARC (v3.2.2) as a reference. The auto-refined maps were then subjected to CTF refinement and manual refinement. The highest resolution used during refinement is indicated in Fig. S4D, I, N, S. Local resolution maps were calculated using RELION⁴³.

The crystal structure of the tryptase-E104.v1 WT complex (PDB: 6VJU)²⁴ was used as an initial model to dock into the cryoEM maps in ChimeraX⁴⁴. The resulting models were rebuilt and refined using COOT (0.9.6), ISOLDE (1.6)⁴⁵, and Phenix (1.21rc1_5049). Sharpened maps were generated using the CryoEM module in COOT (0.9.6). Figures were generated using ChimeraX and PyMOL (2.5.2).

NavAb-Nav1.7 (chimeric) channel. NavAb-Nav1.7-7A9 complexes were prepared by incubating NavAb-Nav1.7 with a 1.2x molar excess of 7A9 Fab at 4 °C for 30 min and separated on a Superose 6 3.2/300 column (Cytiva). Three μL from the peak fraction were applied to Quantifoil R2/2 Au300 holey carbon grids treated with a thiol-reactive, self-assembling reaction mixture of 4 mM monothiolalkane(C11)PEG6-OH (11-mercaptopundecyl) hexaethyleneglycol (SPT-0011P6, SensoPath Technologies Inc., Bozeman, MT)³⁹. Before application of the protein, the grids were removed from the SAM solution and rinsed with ethanol. The grids were blotted in a Vitrobot MarkIV (Thermo Fisher Scientific) at 4 °C and 100% humidity, using a blotting time of 3 s and a blot force of 7, and plunge-frozen in liquid ethane cooled by liquid nitrogen.

Movie stacks were collected using EPU (v3.3.1) on a Titan Krios (Thermo Fisher Scientific) operated at 300 kV and equipped with a Selectris energy filter and a Falcon4 detector. Images were recorded at a magnification of ×165,000 corresponding to 0.731 Å per pixel, using a 20 eV energy slit. Each image stack contains 1077 frames recorded every 0.005 s for an accumulated dose of ~44 e/Å² and a total exposure time of 5 s. Images were recorded with a set defocus range of 0.5 to 1.5 μm.

All image processing was performed in cryoSPARC (v3.2.2), as summarized in Supplementary Fig. 5. Patch motion correction, patch CTF estimation, and particle picking were performed using cryoSPARC Live. Micrographs with CTF fit resolutions worse than 6.5 Å were

rejected. The blob picker was used with a minimum radius of 160 Å and maximum radius of 220 Å. Particles were extracted with a box size of 512 px and binned to 128 px. 2D classification on a small subset of the data was used to identify 2D classes for generation of initial model via ab initio reconstruction. This model was used to generate templates for particle picking with a radius of 220 Å. The resulting particle stack was subjected to 2D classification to remove junk particles. The remaining particles were subjected to iterative rounds of multi-class ab initio reconstruction and heterogeneous refinement. The quality of the particles in the best classes were evaluated by running non-uniform refinement. The particles from the best classes were subjected to 3D classification into 10 classes with a mask around NavAb-Nav1.7 and the Fab variable domain. Classes where the 4-helix bundle was best-resolved were selected and re-extracted with a box size of 512 px and binned to 400 px. Non-uniform refinement of the re-extracted particles led to a consensus 3D reconstruction. Local refinement with a mask around both Fabs was used to improve alignments of the Fabs prior to particle subtraction to remove the Fabs. The signal-subtracted particles were then subjected to local refinement with a mask around NavAb-Nav1.7. Phenix.combine_focused_maps was used to generate a composite map using the consensus map and local refinement maps focused on the Fabs and NavAb-Nav1.7 as inputs. The local resolution of the composite map was calculated using the Local Resolution job in Phenix (1.21rc1_5049) with the composite half maps produced by Phenix.combine_focused_maps.

Structures of the NavAb-Nav1.7-ProTx2-7A9.WT complex (PDB: 6N4Q)²⁶ and NavAb-Nav1.7 (PDB: 5EKO)³⁵ were used as initial models for the 7A9 Fab and NavAb-Nav1.7, respectively, to dock into the cryoEM maps in ChimeraX. The resulting models were rebuilt and refined using COOT (0.9.6), ISOLDE (1.6), and Phenix (1.21rc1_5049). Sharpened maps were generated using the CryoEM module in COOT (0.9.6). Figures were generated using ChimeraX and PyMOL (2.5.2).

CD20. CD20-RTX complexes were prepared by incubating CD20 with a 1.2 molar excess of Fab at 4 °C for 30 min and separated on a Superose 6 3.2/300 column (Cytiva). Three μL from the peak fraction were applied to Quantifoil R0.6/1 Au300 holey carbon grids treated overnight with a thiol-reactive, self-assembling reaction mixture of 4 mM monothiolalkane(C11)PEG6-OH (11-mercaptopundecyl) hexaethyleneglycol (SPT-0011P6, SensoPath Technologies Inc., Bozeman, MT)³⁹. Before application of the protein, the grids were removed from the SAM solution and rinsed with ethanol. The grids were blotted in a Vitrobot MarkIV (Thermo Fisher Scientific) at 4 °C and 100% humidity, using a blotting time of 5 s and a blot force of 8, and plunge-frozen in liquid ethane cooled by liquid nitrogen.

Movie stacks for CD20-RTX.WT were collected from 1 grid using EPU (v3.3.1) on a Titan Krios (Thermo Fisher Scientific) operated at 300 kV and equipped with a Selectris energy filter and a Falcon4 detector. Images were recorded at a magnification of ×165,000 corresponding to 0.731 Å per pixel, using a 20 eV energy slit. Each image stack contains 1011 frames recorded every 0.004 s for an accumulated dose of 37 e/Å² and a total exposure time of 4 s. Images were recorded with a set defocus range of 0.5 to 1.5 μm.

Movie stacks for CD20-RTX.4DS were collected from 4 grids using EPU (v3.3.1) on a Titan Krios (Thermo Fisher Scientific) operated at 300 kV and equipped with a Selectris energy filter and a Falcon4 detector. Images were recorded at a magnification of ×165,000 corresponding to 0.731 Å per pixel, using a 20 eV energy slit. Each image stack contains 1001 frames recorded every 0.005 s for an accumulated dose of 45 e/Å² and a total exposure time of 5 s. Images were recorded with a set defocus range of 0.5 to 1.5 μm.

All image processing was performed in cryoSPARC (v3.2.2), as summarized in Supplementary Fig. 6. Patch motion correction, patch CTF estimation, and particle picking were performed using cryoSPARC Live. Micrographs with CTF fit resolutions worse than 4.0 Å were

rejected. The blob picker was used with a minimum radius of 150 Å and maximum radius of 220 Å. Particles were extracted with a box size of 512 px and binned to 128 px. 2D classification on a small subset of the data was used to identify 2D classes for generation of initial model via ab initio reconstruction. This model was used to generate templates for particle picking with a radius of 200 Å. The resulting particle stack was subjected to 2D classification to remove junk particles. The remaining particles were subjected to iterative rounds of multi-class ab initio reconstruction and heterogeneous refinement. The quality of the particles in the best classes were evaluated by running non-uniform refinement. These particles from the best classes were re-extracted with a box size of 512 px and binned to 400 px. Non-uniform refinement of the re-extracted particles led to a consensus 3D reconstruction. Local refinement was performed with a mask around the variable domains of both Fabs and CD20. The fulcrum for the local refinement was also shifted to the center of mass for the CD20 portion of the structure. The resulting volume was used as input for another local refinement with a mask around only CD20. Phenix.combine_focused_maps was used to generate a composite map using the consensus map and local refinement maps as inputs. The local resolution of the composite map was calculated using the Local Resolution job in Phenix (1.21rc1_5049) with the composite half maps produced by Phenix.combine_focused_maps.

The model for the structure of the CD20-RTX.WT complex (PDB: 6VJA)²⁷ was used as an initial model to dock into the cryoEM maps in ChimeraX. The resulting models were rebuilt and refined using COOT (0.9.6), ISOLDE (1.6), and Phenix (1.21rc1_5049). Sharpened maps were generated using the CryoEM module in COOT (0.9.6). Figures were generated using ChimeraX and PyMOL (2.5.2).

Ang2. Ang2 was incubated with an equimolar amount of the (1) 5A12.6DS Fab and a 2-fold molar excess of ProA-ProG fusion protein, (2) 5A12.6DS Fab only, (3) 5A12.WT Fab only, on ice for 30 min to prepare the various samples. This mixture was injected onto a Superdex 200 3.2/300 column equilibrated in 20 mM HEPES pH 7.5, 150 mM NaCl. The peak fraction was subjected to mild crosslinking with 0.5 mM BS3 at room temperature for 10 min. The crosslinking reaction was quenched by addition of 100 mM Tris pH 7.5. CryoEM grids of each sample were prepared identically: 4 µL of sample were applied to glow-discharged Quantifoil R0.6/1 Au300 holey carbon grids, blotted in a Vitrobot MarkIV at 4 °C and 100% humidity using a blotting time of 6 s and a blot force of 7, and plunge-frozen in liquid ethane cooled by liquid nitrogen.

Movie stacks were collected using SerialEM (v4.1.0)40 on a Titan Krios (Thermo Fisher Scientific) operated at 300 kV and equipped with a BioQuantum energy filter operated with a 20 eV energy slit with a K3 Summit direct electron detector camera (Gatan). Ang2-5A12.6DS Fab images were recorded in EFTEM mode at a magnification of $\times 105,000$ corresponding to 0.838 Å per pixel, using a 20 eV energy slit. Each image stack contains 119 frames recorded every 0.05 s for an accumulated dose of 69 e/Å² and a total exposure time of 6 s. Images for the 6DS Fab vs. WT comparison were collected at a magnification of $\times 165,000$ corresponding to 0.731 Å per pixel, with an accumulated dose of 46 e/Å² fractionated over 80 frames. All images were recorded with a set defocus range of 0.5 to 1.5 µm.

All image processing was performed using cryoSPARC (v3.2.2) as summarized in the schematic in Supplementary Figs. 7 and 8. Patch motion correction, patch CTF estimation, and particle picking were performed using cryoSPARC Live. For the Ang2-5A12.6DS Fab dataset (Supplementary Fig. 7), micrographs with CTF fit resolutions worse than 3.7 Å or with relative ice thickness higher than 1.077 were rejected. For the datasets used in the 6DS Fab vs. WT comparison (Supplementary Fig. 8), the CTF selection threshold was set to 7.0 Å, and 0.9–1.15 for the ice thickness. The blob picker was used with a minimum radius of 50 Å and maximum radius of 150 Å, using both a circular

blob and elliptical blob, as well as a minimum separation distance of 0.3 diameters. Particles were extracted with a box size of 400 px and binned to 128 px. 2D classification of a small subset of the data was performed to identify 2D classes for generation of initial model via ab initio reconstruction. This model was used to generate templates for particle picking with a radius of 100 Å. The resulting particle stack was subjected to 2D classification to remove junk particles. The remaining particles were subjected to iterative rounds of multi-class ab initio reconstruction and heterogeneous refinement. The Ang2-5A12.6DS Fab dataset, retained 1,017,611 particles, while the 6DS Fab vs. WT datasets retained 66,000 and 20,000 particles, respectively. To ensure a fair comparison, only 20,000 of the 66,000 of the 6DS Fab particles were used. The particles were re-extracted with a box size of 400 px and binned to 324 px. These particles were then subjected to non-uniform refinement, resulting in a 3D reconstruction with a GS-FSC resolution of 2.7 Å for the Ang2-5A12.6DS Fab dataset, and 3.3 Å and 3.7 Å for the 6DS Fab and WT datasets, respectively. The 6DS Fab vs. WT maps were further refined locally to exclude the constant domain of the Fab, which is expected to be flexible in the WT data. Local resolution maps were calculated using the Local Resolution Estimation job in cryoSPARC (v3.2.2).

The crystal structure of the Ang2-5A12.WT complex (PDB: 4ZFG)²⁸ was used as an initial model to dock into the cryoEM map for the Ang2-5A12.6DS Fab complex in ChimeraX. The resulting model was rebuilt and refined using COOT (0.9.6), ISOLDE (1.6), and Phenix (1.21rc1_5049). Sharpened maps were generated using the CryoEM module in COOT (0.9.6). Figures were generated using ChimeraX and PyMOL (2.5.2).

KRAS^{G12C}. KRAS^{G12C} was covalently modified with GNE-1952²⁹. KRAS^{G12C} was incubated for 4 h at room temperature with 150 µM GNE-1952, 5 mM GDP, and 20 mM EDTA. Complete covalent modification was confirmed via mass spectrometry. The modified protein was then buffer exchanged into 20 mM HEPES pH 7.0, 100 mM NaCl, 1 mM MgCl₂, 5 µM GDP through size exclusion chromatography on a Superdex 75 16/60 column (Cytiva). The KRAS^{G12C}-GNE-1952 adduct was incubated with a 2-fold molar excess of the 2H11.4DS Fab on ice for 30 min. This mixture was then injected onto a Superdex 200 3.2/300 column equilibrated in 20 mM HEPES pH 7.0, 100 mM NaCl, 1 mM MgCl₂, 5 µM GDP. The peak fraction was subjected to mild crosslinking with 0.5 mM BS3 at room temperature for 10 min. Four µL of this sample were then applied to glow-discharged Quantifoil R0.6/1 Au300 holey carbon grids, blotted in a Vitrobot MarkIV at 4 °C and 100% humidity using a blotting time of 6 s and a blot force of 7, and plunge-frozen in liquid ethane cooled by liquid nitrogen.

Movie stacks were collected using EPU (v3.3.1) on a Titan Krios (Thermo Fisher Scientific) operated at 300 kV and equipped with a Selectris energy filter and a Falcon4 detector. Images were recorded at a magnification of $\times 165,000$ corresponding to 0.731 Å per pixel, using a 20 eV energy slit. Each image stack contains 1077 frames recorded every 0.005 s for an accumulated dose of 40 e/Å² and a total exposure time of 2.2 s. Images were recorded with a set defocus range of 0.5 to 1.5 µm.

All image processing was performed using cryoSPARC (v4.1) as summarized in the schematic in Supplementary Fig. S9. Patch motion correction, patch CTF estimation, and particle picking were performed using cryoSPARC Live. Micrographs with CTF fit resolutions worse than 4.0 Å or with relative ice thickness higher than 1.12 were rejected. The blob picker was used with a minimum radius of 50 Å and maximum radius of 150 Å, using both a circular blob and elliptical blob, as well as a minimum separation distance of 0.5 diameters. Particles were extracted with a box size of 324 px and binned to 128 px. 2D classification of a small subset of the data was performed to identify 2D classes for generation of initial model via ab initio reconstruction. This

model was used to generate templates for particle picking with a radius of 150 Å. The resulting particle stack was subjected to 2D classification to remove junk particles. The remaining particles were subjected to iterative rounds of multi-class ab initio reconstruction and heterogeneous refinement, resulting in a stack of 926,738 particles, which were re-extracted with a box size of 324 px and binned to 224 px. These particles were then subjected to non-uniform refinement, including refinement of per-particle defocus and per-group CTF parameters (tilt and trefoil), resulting in a 3D reconstruction with a GS-FSC resolution of 2.83 Å. Local refinement was then performed using a mask around KRAS and the 2H11.4DS variable domain, leading to a 3D reconstruction with a GS-FSC resolution of 2.74 Å. Local resolution maps were calculated using the Local Resolution Estimation job in cryoSPARC (v4.1).

The crystal structure of the KRAS^{G12C}-GNE-1952-2H11.WT complex (PDB: 7RP3)²⁹ was used as an initial model to dock into the cryoEM maps in ChimeraX. The resulting model was rebuilt and refined using COOT (0.9.6), ISOLDE (1.6), and Phenix (1.21rc1.5049). Sharpened maps were generated using the CryoEM module in COOT (0.9.6). Figures were generated using ChimeraX and PyMOL (2.5.2).

Reporting summary

Further information on research design is available in the Nature Portfolio Reporting Summary linked to this article.

Data availability

The data that support this study are available from the corresponding authors upon request. Coordinates and related data for the crystal structures of the E104.v1.4DS.S112F, E104.v1.4DS.A114F, E104.v1.5DS, and E104.v1.6DS have been deposited in the PDB with the following accession codes, respectively: [8VEG](#), [8VGE](#), [8VGF](#), and [8VGG](#). Coordinates and cryoEM maps for the structures of trypsin in complex with E104.v1.WT, E104.v1.2DS, E104.v1.4DS, and E104.v1.6DS have been deposited in the PDB and EMDB with the following accession codes, respectively: [8VGH/EMD-43200](#), [8VGI/EMD-43201](#), [8VGJ/EMD-43202](#), and [8VGK/EMD-43203](#). Coordinates and cryoEM maps for the structure of NavAb-Nav1.7 in complex with wild type 7A9 Fab have been deposited in the PDB and EMDB with the following accession codes: [8VGL](#) (model), [EMD-43204](#) (composite map), [EMD-43205](#) (consensus map), [EMD-43206](#) (focused refinement of 7A9 Fab), and [EMD-43207](#) (focused refinement of NavAb-Nav1.7). Coordinates and cryoEM maps for the structure of NavAb-Nav1.7 in complex with 7A9.4DS Fab have been deposited in the PDB and EMDB with the following accession codes: [8VGM](#) (model), [EMD-43208](#) (composite map), [EMD-43209](#) (consensus map), [EMD-43210](#) (focused refinement of 7A9 Fab), and [EMD-43211](#) (focused refinement of NavAb-Nav1.7). Coordinates and cryoEM maps for the structure of CD20 in complex with wild type Rituximab Fab have been deposited in the PDB and EMDB with the following accession codes: [8VGN](#) (model), [EMD-43212](#) (composite map), [EMD-43213](#) (consensus map), [EMD-43214](#) (focused refinement of Fab variable domain and CD20), and [EMD-43215](#) (focused refinement of CD20). Coordinates and cryoEM maps for the structure of CD20 in complex with Rituximab.4DS Fab have been deposited in the PDB and EMDB with the following accession codes: [8VGO](#) (model), [EMD-43216](#) (composite map), [EMD-43217](#) (consensus map), [EMD-43218](#) (focused refinement of Fab variable domain and CD20), and [EMD-43219](#) (focused refinement of CD20). Coordinates and cryoEM maps for the structure of Ang2 in complex with 5A12.6DS have been deposited in the PDB and EMDB with the following accession codes: [8VGP](#), [EMD-43220](#). CryoEM maps for the comparison between 5A12.6DS and 5A12.WT Fabs in complex with Ang2 have been deposited in the EMDB with the following accession codes: [EMD-71531](#) (6DS) and [EMD-71532](#) (WT). Coordinates and cryoEM maps for the structure of KRAS G12C in complex with 2H11.4DS have been deposited in the PDB and EMDB with the following accession codes: [8VGQ](#), [EMD-43221](#). Exposure-

fractionated micrographs for the following datasets were deposited to EMPIAR: Ang2:6DS-Fab [<https://www.ebi.ac.uk/empair/EMPIAR-12290/>] (EMPIAR-12290), KRAS:4DS-Fab (EMPIAR-12289) [<https://www.ebi.ac.uk/empair/EMPIAR-12289/>].

References

- Kühlbrandt, W. The resolution revolution. *Science* **343**, 1443–1444 (2014).
- Wu, M. & Lander, G. C. How low can we go? Structure determination of small biological complexes using single-particle cryo-EM. *Curr. Opin. Struct. Biol.* **64**, 9–16 (2020).
- Yeates, T. O., Agdanowski, M. P. & Liu, Y. Development of imaging scaffolds for cryo-electron microscopy. *Curr. Opin. Struct. Biol.* **60**, 142–149 (2020).
- Yao, Q., Weaver, S. J., Mock, J.-Y. & Jensen, G. J. Fusion of DARPin to aldolase enables visualization of small protein by cryo-EM. *Structure* <https://doi.org/10.1016/j.str.2019.04.003> (2019).
- Liu, Y., Huynh, D. T. & Yeates, T. O. A 3.8 Å resolution cryo-EM structure of a small protein bound to an imaging scaffold. *Nat. Commun.* **10**, 1864 (2019).
- Robertson, M. J. et al. Structure determination of inactive-state GPCRs with a universal nanobody. *Nat. Struct. Mol. Biol.* **29**, 1188–1195 (2022).
- Castells-Graells, R. et al. Cryo-EM structure determination of small therapeutic protein targets at 3 Å-resolution using a rigid imaging scaffold. *Proc. Natl. Acad. Sci. USA* **120**, e2305494120 (2023).
- Bloch, J. S. et al. Development of a universal nanobody-binding Fab module for fiducial-assisted cryo-EM studies of membrane proteins. *Proc. Natl. Acad. Sci.* **118**, e2115435118 (2021).
- Botte, M. et al. Cryo-EM structures of a LptDE transporter in complex with Pro-macrobodies offer insight into lipopolysaccharide translocation. *Nat. Commun.* **13**, 1826 (2022).
- Jones, S. A. et al. Structural basis of purine nucleotide inhibition of human uncoupling protein 1. *Sci. Adv.* **9**, eadh4251 (2023).
- Bailey, L. J. et al. Locking the elbow: improved antibody Fab fragments as chaperones for structure determination. *J. Mol. Biol.* **430**, 337–347 (2018).
- Sauer, D. B. et al. Structural basis for the reaction cycle of DASS dicarboxylate transporters. *eLife* **9**, e61350 (2020).
- Wu, X. & Rapoport, T. A. Cryo-EM structure determination of small proteins by nanobody-binding scaffolds (Legobodies). *Proc. Natl. Acad. Sci. USA* **118**, e2115001118 (2021).
- Uchański, T. et al. Megabodies expand the nanobody toolkit for protein structure determination by single-particle cryo-EM. *Nat. Methods* **18**, 60–68 (2021).
- Vulovic, I. et al. Generation of ordered protein assemblies using rigid three-body fusion. *Proc. Natl. Acad. Sci. USA* **118**, e2015037118 (2021).
- Henderson, R. The potential and limitations of neutrons, electrons and X-rays for atomic resolution microscopy of unstained biological molecules. *Q. Rev. Biophys.* **28**, 171–193 (1995).
- Wu, S. et al. Fabs enable single particle cryoEM studies of small proteins. *Structure* **20**, 582–592 (2012).
- Stanfield, R. L., Zemla, A., Wilson, I. A. & Rupp, B. Antibody elbow angles are influenced by their light chain class. *J. Mol. Biol.* **357**, 1566–1574 (2006).
- Zhang, Z. et al. Ensemble cryoEM elucidates the mechanism of insulin capture and degradation by human insulin degrading enzyme. *eLife* **7**, e33572 (2018).
- Lopez-Redondo, M. et al. Zinc binding alters the conformational dynamics and drives the transport cycle of the cation diffusion facilitator YiiP. *J. Gen. Physiol.* **153**, e202112873 (2021).
- Brawley, D. N. et al. Structural basis for inhibition of the drug efflux pump NorA from *Staphylococcus aureus*. *Nat. Chem. Biol.* **18**, 706–712 (2022).

22. Kintzer, A. F. et al. Structural basis for activation of voltage sensor domains in an ion channel TPC1. *Proc. Natl. Acad. Sci. USA* **115**, E9095–E9104 (2018).
23. Popkov, M. et al. Rabbit immune repertoires as sources for therapeutic monoclonal antibodies: the impact of kappa allotype-correlated variation in cysteine content on antibody libraries selected by phage display. *J. Mol. Biol.* **325**, 325–335 (2003).
24. Maun, H. R. et al. Bivalent antibody pliers inhibit β -tryptase by an allosteric mechanism dependent on the IgG hinge. *Nat. Commun.* **11**, 6435 (2020).
25. Stagg, S. M., Noble, A. J., Spilman, M. & Chapman, M. S. ResLog plots as an empirical metric of the quality of cryo-EM reconstructions. *J. Struct. Biol.* **185**, 418–426 (2014).
26. Xu, H. et al. Structural basis of Nav1.7 inhibition by a gating-modifier spider toxin. *Cell* **176**, 702–715.e14 (2019).
27. Rougé, L. et al. Structure of CD20 in complex with the therapeutic monoclonal antibody rituximab. *Science* **367**, 1224–1230 (2020).
28. Koenig, P. et al. Deep sequencing-guided design of a high affinity dual specificity antibody to target two angiogenic factors in neovascular age-related macular degeneration*. *J. Biol. Chem.* **290**, 21773–21786 (2015).
29. Davies, C. W. et al. Conformation-locking antibodies for the discovery and characterization of KRAS inhibitors. *Nat. Biotechnol.* **40**, 769–778 (2022).
30. Jumper, J. et al. Highly accurate protein structure prediction with AlphaFold. *Nature* **596**, 583–589 (2021).
31. Evans, R. et al. Protein complex prediction with AlphaFold-Multimer. *bioRxiv* <https://doi.org/10.1101/2021.10.04.463034> (2022).
32. Wohlwend, J. et al. Boltz-1 democratizing biomolecular interaction modeling. *bioRxiv* <https://doi.org/10.1101/2024.11.19.624167> (2024).
33. Terwilliger, T. C. et al. AlphaFold predictions are valuable hypotheses and accelerate but do not replace experimental structure determination. *Nat. Methods* **21**, 110–116 (2024).
34. Maun, H. R. et al. Dual functionality of β -tryptase protomers as both proteases and cofactors in the active tetramer. *J. Biol. Chem.* **293**, 9614–9628 (2018).
35. Ahuja, S. et al. Structural basis of Nav1.7 inhibition by an isoform-selective small-molecule antagonist. *Science* **350**, aac5464 (2015).
36. Kabsch, W. & IUCr. Xds. *Acta Crystallogr. Sect. D Biol. Crystallogr.* **66**, 125–132 (2010).
37. Emsley, P., Lohkamp, B., Scott, W. G. & Cowtan, K. Features and development of Coot. *Acta Crystallogr. Sect. D* **66**, 486–501 (2010).
38. Liebschner, D. et al. Macromolecular structure determination using X-rays, neutrons and electrons: recent developments in Phenix. *Acta Crystallogr. Sect. D* **75**, 861–877 (2019).
39. Meyerson, J. R. et al. Self-assembled monolayers improve protein distribution on holey carbon cryo-EM supports. *Sci. Rep.* **4**, 7084 (2014).
40. Mastronarde, D. N. Automated electron microscope tomography using robust prediction of specimen movements. *J. Struct. Biol.* **152**, 36–51 (2005).
41. Grant, T., Rohou, A. & Grigorieff, N. cisTEM, user-friendly software for single-particle image processing. *eLife* **7**, e35383 (2018).
42. Punjani, A., Rubinstein, J. L., Fleet, D. J. & Brubaker, M. A. cryoSPARC: algorithms for rapid unsupervised cryo-EM structure determination. *Nat. Methods* **14**, 290–296 (2017).
43. Scheres, H. & Sjors, W. RELION: implementation of a Bayesian approach to cryo-EM structure determination. *J. Struct. Biol.* **180**, 519–530 (2012).
44. Pettersen, E. F. et al. UCSF ChimeraX: structure visualization for researchers, educators, and developers. *Protein Sci.* **30**, 70–82 (2020).
45. Croll, T. I. ISOLDE: a physically realistic environment for model building into low-resolution electron-density maps. *Acta Crystallogr. Sect. D Struct. Biol.* **74**, 519–530 (2018).

Acknowledgements

The authors would like to thank the Antibody Engineering, Protein Chemistry, Biomolecular Resources Departments and the cryoEM team at Genentech for their support in generating constructs, protein purification, and data collection; Henry Maun for conversations on Tryptase protein production; and Stanford Synchrotron Radiation Lightsource (SSRL) and Advanced Light Source (ALS) for access to the synchrotrons. Use of the Stanford Synchrotron Radiation Lightsource, SLAC National Accelerator Laboratory, is supported by the US Department of Energy, Office of Science, Office of Basic Energy Sciences under Contract No. DE-AC02-76SF00515. The SSRL Structural Molecular Biology Program is supported by the DOE Office of Biological and Environmental Research, and by the National Institutes of Health, National Institute of General Medical Sciences (P41GM103393). The contents of this publication are solely the responsibility of the authors and do not necessarily represent the official views of NIGMS or NIH. Beamline 5.0.2 of the Advanced Light Source, a DOE Office of Science User Facility under Contract No. DE-AC02-05CH11231, is supported in part by the ALS-ENABLE program funded by the National Institutes of Health, National Institute of General Medical Sciences, grant P30 GM124169-01.

Author contributions

J.E.K. and J.S. conceived and designed protein engineering strategies and experiments to generate and characterize Rigid Fabs. J.E.K. performed recombinant protein production, binding assays, crystallization, cryoEM sample and grid preparation, and solved structures. A.O. and P.W. generated antigen-Fab complex samples for cryoEM. M.L. and J.M.D. purified WT and Rigid Fabs. M.C.J. and C.P.A. performed grid preparation and optimization, cryoEM data collection, and assisted in data processing. C.M.K. advised on selection of membrane proteins for assessing rigidity of Rigid Fab designs across species and chimeras. C.C.J. prepared protein samples for CD20 and NavAb-Nav1.7 complexes. D.T. performed data processing for comparing WT and Rigid Fab structures of Ang2. D.T. and A.R. advised on experimental designs and cryoEM data processing strategies. J.E.K. and J.S. analyzed all data and wrote the manuscript with input from all authors.

Competing interests

All authors are current or former employees of Genentech, Inc.

Additional information

Supplementary information The online version contains supplementary material available at <https://doi.org/10.1038/s41467-025-63766-8>.

Correspondence and requests for materials should be addressed to Jawahar Sudhamsu.

Peer review information *Nature Communications* thanks the anonymous reviewers for their contribution to the peer review of this work. A peer review file is available.

Reprints and permissions information is available at <http://www.nature.com/reprints>

Publisher's note Springer Nature remains neutral with regard to jurisdictional claims in published maps and institutional affiliations.

Open Access This article is licensed under a Creative Commons Attribution-NonCommercial-NoDerivatives 4.0 International License, which permits any non-commercial use, sharing, distribution and reproduction in any medium or format, as long as you give appropriate credit to the original author(s) and the source, provide a link to the Creative Commons licence, and indicate if you modified the licensed material. You do not have permission under this licence to share adapted material derived from this article or parts of it. The images or other third party material in this article are included in the article's Creative Commons licence, unless indicated otherwise in a credit line to the material. If material is not included in the article's Creative Commons licence and your intended use is not permitted by statutory regulation or exceeds the permitted use, you will need to obtain permission directly from the copyright holder. To view a copy of this licence, visit <http://creativecommons.org/licenses/by-nc-nd/4.0/>.

© The Author(s) 2025